IEEE Access
Multidisciplinary | Rapid Review | Open Access Journal

Received April 14, 2019, accepted April 26, 2019, date of publication May 1, 2019, date of current version May 14, 2019.

Digital Object Identifier 10.1109/ACCESS.2019.2914319

Simultaneous Arteriole and Venule Segmentation of Dual-Modal Fundus Images Using a Multi-Task Cascade Network

SHULIN ZHANG[1], RUI ZHENG[1], YUHAO LUO[1], XUEWEI WANG[1], JIANBO MAO[2], CYNTHIA J. ROBERTS[3], AND MINGZHAI SUN[1]

[1]Department of Precision Machinery and Instrumentation, University of Science and Technology of China, Hefei 230026, China
[2]Eye Hospital of Wenzhou Medical University, Wenzhou Medical University, Wenzhou 325035, China
[3]Department of Ophthalmology and Visual Science, The Ohio State University, Columbus, OH 43212, USA

Corresponding author: Mingzhai Sun (mingzhai@ustc.edu.cn)

This work was supported in part by the Fundamental Research Funds for the Central Universities under Grant WK2090090023, and in part by the Medical Health Science and Technology Project of Zhejiang Provincial Health Commission under Grand 2019PY010.

ABSTRACT Differentiating arterioles and venules in the fundus image is important for not only various eye diseases but also systemic diseases such as hypertension and ischemic stroke. In this paper, we use dual-modal fundus images and develop a cascade refined U-net (CRU-net) to improve the arteriovenous segmentation. In this paper, dual-modal fundus images include not only a regular color fundus image (RGB image) but also another two monochromic images acquired using two different wavelengths, 570 and 610 nm. The choice of these two wavelengths is based on the absorption spectra of hemoglobin. The two monochromic images provide much richer information on the arteriole and venule. Our proposed CRU-net can fully utilize the information and achieves the state-of-the-art performance on our dual-modal dataset (DualModal2019). The arteriovenous classification accuracy evaluated on the automatically detected vessels is 97.27%, significantly surpassed previous methods. The F1-scores are 77.69% and 79.53% for the arteriole and venule segmentation, respectively. We also test our CRU-net on the public DRIVE dataset with only the color fundus images. We achieve the accuracy of 93.97%, F1-scores of 73.50%, and 75.54% for the arteriole and venule, all of which significantly surpassed previously published methods. Our DualModal2019 dataset with manually annotated arterioles and venules is publicly available.

INDEX TERMS Dual-modal fundus image, arteriovenous segmentation, deep convolutional neural network (DCNN), cascade refined U-net (CRU-net).

I. INTRODUCTION

The morphology of retinal blood vessels is associated with various ophthalmic and systemic diseases [1]–[3]. Retinal images have been used to diagnose conditions such as diabetic retinopathy [3], glaucoma [4], narrowing arteriole [1], age-related macular degeneration (AMD) [5], arteriosclerosis and hypertension [6], etc. These diseases have varying effects on arterioles and venules. Some affect specifically the arteriole or the venule. For example, the coronary arterial disease is indicated by the decreased arteriole caliber [7]; hypertensive retinopathy is suggested by the arteriole narrowing at the early stage [8], and diseases of the pancreas lead to narrowed arteriole [9]. Other conditions affect venules. For example, increased venular caliber is associated with diabetic retinopathy and risk of stroke [3]. Diseases may also affect the arteriole and venule to varying degrees, which leads to the change of the ratio between the calibers of arteriole and venule (AVR). AVR [10] is commonly used as an important diagnostic indicator of various associated diseases. For example, high cholesterol levels or high blood pressure causes abnormal AVR [11].

Evident from the situations above, the arteriovenous analysis is important for the diagnosis of different diseases. Most of the published retinal arteriovenous studies are based on RGB images (Fig 1). The morphological structure of the arteriole

The associate editor coordinating the review of this manuscript and approving it for publication was Shagufta Henna.

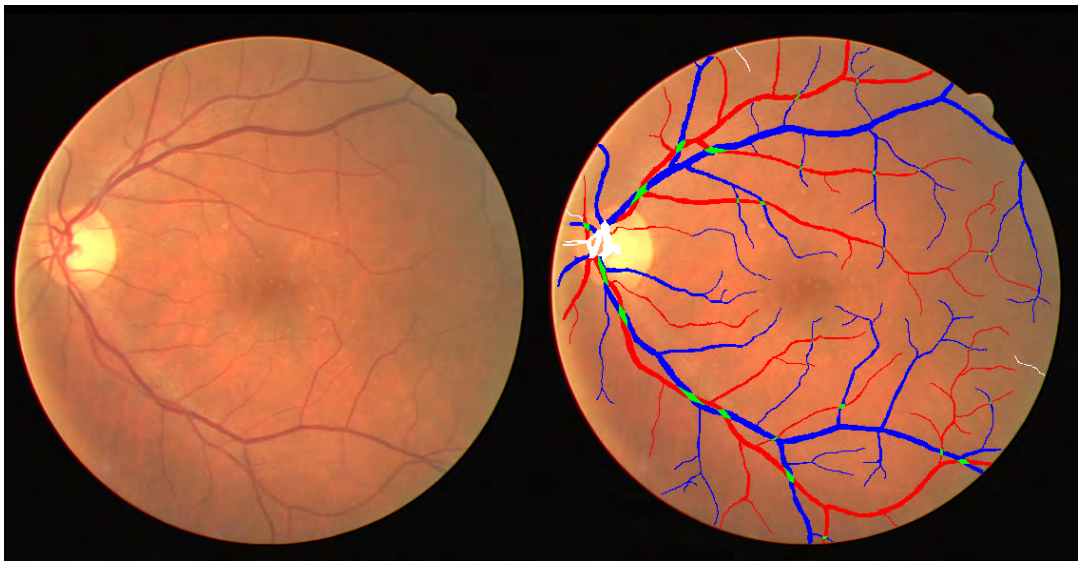

FIGURE 1. A typical color fundus image (left) with annotated arterioles and venules (right) from the DRIVE dataset. The blue and red color mark the venule and arteriole, respectively. Intersections between the venule and arteriole are marked green. White color labels the uncertain segmentations.

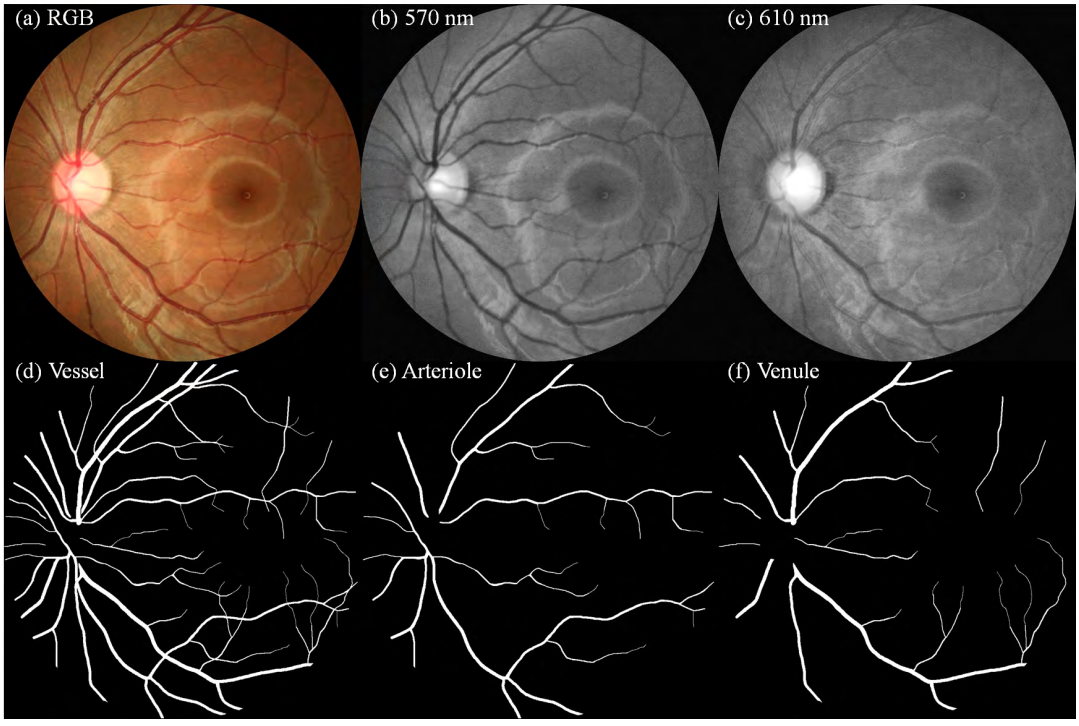

FIGURE 2. A typical dual-modal image set from the DualModal2019 dataset. (a) RGB color image, (b) the grayscale images acquired at 570 nm and 610 nm (c). (d-f) manually annotated ground truth images for the vessels, arterioles, and venules.

and venule is very similar, and the contrast, particularly at the distant part is very low on the RGB image (Fig 1), making it prone to misclassification of the venules and arterioles.

Recently, dual-modal fundus imaging technique has been applied to the diagnosis of retinal diseases (Fig 2). In addition to the RGB image, dual-modal fundus camera applies two monochromatic wavelengths (570 nm and 610 nm in our study) to image the retina. These two wavelengths are chosen based on the absorption spectra of hemoglobin. The oxyhemoglobin and deoxyhemoglobin share nearly the same extinction coefficient at 570 nm, while they have significant differences at 610 nm where oxyhemoglobin has little absorption [12]. The differences result in clear visibility of both arterioles and venules at 570 nm, but much less visibility of arterioles than venules at 610 nm (Fig 2(b), (c)). Full utilization of the different visibility of arterioles and

venules at the two wavelengths can significantly improve the arteriovenous analysis.

In this study, we combine RGB, 570 nm and 610 nm images and fully utilize the rich information of the dual-modal images. We propose a new segmentation network, a cascade refined U-net (CRU-net), to detect and segment arterioles and venules. The CRU-net takes full advantage of the three image types to promote performance. Besides, the CRU-net shows superior performance on conventional fundus images (RGB images).

The main contributions of the study are: 1) we develop a CRU-net, which takes advantages of the dual-modal retinal images, to achieve the state-of-the-art performance in arteriole and venule segmentation; 2) we systemically demonstrate that dual-modal retinal images provide richer information about the venules and arterioles, which significantly improves the arteriovenous analysis by comparing with single-modal retinal image (RGB only) analysis; 3) we make the dual-modal fundus image dataset, DualModal2019, together with the annotated ground truth images, publicly available so that other researchers can explore it.

II. RELATED WORK

The studies on arteriole and venule segmentation can be mainly grouped into two categories: feature-based and graph-based methods. The feature-based methods classify target pixels by capturing features from fundus image patches centered on the target pixel. They usually share several common steps. The first step is to obtain the segmentation of the vasculature tree or to start with it directly. Next, the vessel centerlines were extracted from the vasculature. Finally, these vessel segments were classified into arteriole or venule by the features extracted from their status or the type of centerline pixels belonging to them. Welikala *et al.* [13] applied profile-based and region-of-interest-based feature extraction methods and two other classification methods based on support vector machines and neural networks to classify arteriole and venule. The idea in [14] is to justify the balanced layout of arteriole and venule in retinal fundus by the local nature of the classification process.

There is also much progress in graph-based approaches. Rothaus *et al.* [15] developed an automated graph separation algorithm to distinguish between arterioles and venules in retinal images. Dashtbozorg [16] proposed a three-step method. The first step is to classify the entire vascular tree deciding on the type of each intersection point (graph nodes) and the second is assigning one of two labels to each vessel segment (graph links). Final classification of a vessel segment as arteriole and venule is performed through the combination of the graph-based labeling results with a set of intensity features.

Deep learning approaches have been successfully applied in many medical image analysis system, like detection of the brain tumors [17], breast nodules, lesions from ultrasound images [18], and Alzheimer disease from brain MRIs [19]. Deep learning was also applied in fundus image analysis, such as exudates segmentation [20], and arteriovenous segmentation. Hemelings *et al.* [21] and Xu *et al.* [22] applied improved U-net [23] to segment the arteriole and venule simultaneously and evaluated their performance on DRIVE dataset. Meyer *et al.* [24] used an FCN with a loss function which only focused on the pixels of vasculature regardless of the background pixels of the fundus image to adapt for arteriole/venule classification. Albadawi and Fraz [25] applied SegNet [26] based fully convolutional deep neural network for pixel level classification of the retinal pixel into arteriole, venule, and background.

The information from dual-modal images is much richer than the information from the RGB image only. However, richer information also puts forward higher requirements for feature extraction ability of the network. Currently, there are no deep-learning based studies on arteriovenous segmentation using dual-modal fundus images. To this end, we propose a cascade refined U-net network (CRU-net) to fully utilize the dual-modal fundus image information for retinal arteriovenous segmentation. In order to compare our proposed network with previous studies, we evaluate our method both on the publicly available DRIVE dataset and our own dual-modal fundus images dataset (DualModal2019 dataset). The performance of CRU-net exceeds the highest level of existing literature on the vessel, venule, and arteriole segmentation.

III. METHOD

A. DATASETS

Two datasets were applied in the study. One is the publicly available DRIVE [27] dataset, and the other is our own dual-modal fundus image dataset (DualModal2019), which we make publicly available with manually annotated ground truth images of the arterioles and venules.

DRIVE dataset consists of 40 fundus images with a resolution of 565 × 584 pixels. The arteriovenous annotations of the database are provided by [28].

The DualModal2019 dataset has 30 sets of images with a resolution of 1024 × 1024 pixels. Each set of images comprises three images: RGB color image and the corresponding 570 nm and 610 nm monochromic images as illustrated in Fig. 2. All the dual-modal fundus images were acquired with a dual-modal fundus camera (OT-110M, Hefei Orbis Biotech LTD, China). The camera provides a field of view of 45° using a xenon lamp as the light source. It captures images of 570 nm, 610 nm and RGB channels simultaneously. The three images are aligned automatically with the provided software. All the images were acquired from 16 healthy volunteers aged from 20-30 years old with no sign of retinal diseases. For 14 volunteers, images from both eyes (left and right eyes) were acquired, while for the other 2 volunteers, images from only one eye were chosen because of the poor image quality from the other eye. The ground truth images for the vessels, arterioles, and venules were manually annotated for the corresponding RGB, 570 nm and

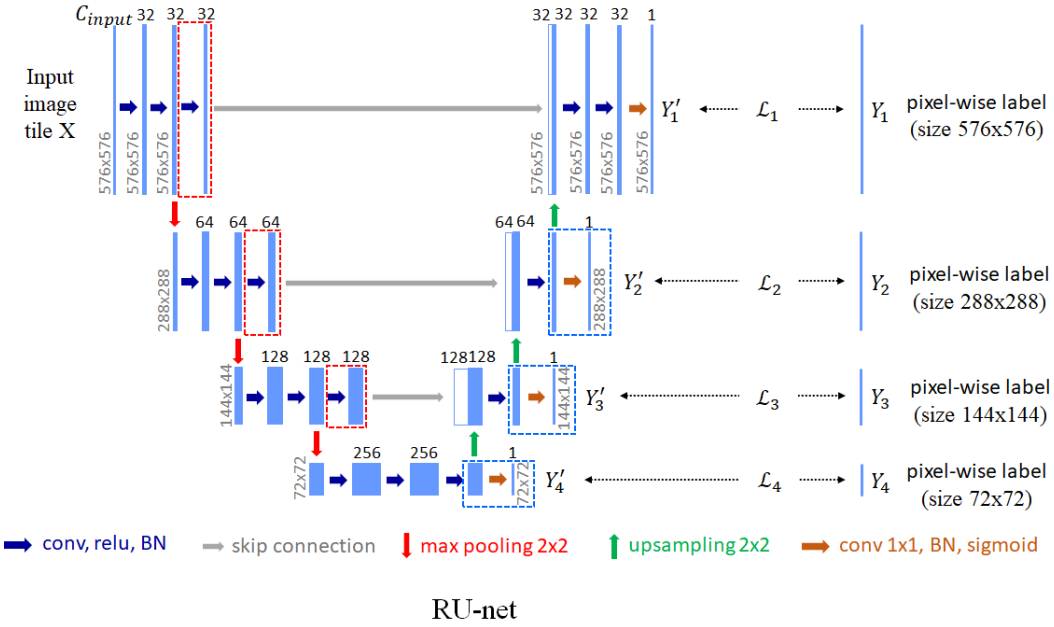

FIGURE 3. Structure of the RU-net. Y_i and Y_i' are the resized ground truth image and the predicted image; $\mathcal{L}_i$ represents the loss term between Y_i and Y_i'.

TABLE 1. Configuration of the RU-net.

Feature size	Encode path	Skip path	Decode path	Segmentation map
576x576	Conv2D 32 3x3		Conv2D 16 3x3	Conv2D 1 3x3
576x576	Conv2D 32 3x3	Conv2D 32 3x3	concate(axis=3)	
	MaxPooling2D 2x2		UpSampling2D	
288x288	Conv2D 64 3x3		Conv2D 32 3x3	Conv2D 1 3x3
288x288	Conv2D 64 3x3	Conv2D 64 3x3	concate(axis=3)	
	MaxPooling2D 2x2		UpSampling2D	
144x144	Conv2D 128 3x3		Conv2D 64 3x3	Conv2D 1 3x3
144x144	Conv2D 128 3x3	Conv2D 128 3x3	concate(axis=3)	
	MaxPooling2D 2x2		UpSampling2D	
72x72	Conv2D 256 3x3	Conv2D 256 3x3	Conv2D 128 3x3	Conv2D 1 3x3

610 nm images with the help of an ophthalmologist. During training, 24 sets of images were used as the training dataset and 6 sets of images were applied as the testing dataset. However, to ensure complete independence of the training and testing data, images of the left and right eyes from the same volunteer are assigned into the same dataset, either the training or the testing dataset. There is no situation that images of the left eye are assigned in the training dataset while images of the right eyes are in the testing dataset or vice versa. We make the DualModal2019 dataset publicly available with clear identification of the images with the subject id and identification of right and left eyes.

B. RU-NET

We developed a refined U-net (RU-net) based on the inspiration from the U-net and the label refinement network (LRN) [23], [29]. As shown in Fig. 3, the RU-net is an encoder-decoder architecture, with the detailed configuration listed in Table. 1. The novelties of the RU-net lie in the concatenation module and the multi-scale loss evaluation. Different from the original U-net, the RU-net applies an additional convolutional layer before concatenating with the corresponding decoder layer, as shown in the red dotted rectangles in Fig. 3. Four loss functions of different scales are evaluated at the decoder path. The total loss is the sum of all the four multi-scale losses. We applied a class-balanced loss function for each loss term by comparing the semantic segmentation map with the corresponding ground truth image. The total loss of RU-net is defined as:

$$\begin{aligned}\mathcal{L}_{task}(Y|X;\theta) = {} & k_1 \cdot \mathcal{L}_1(Y_1', Y_1|X;\theta) \\ & + k_2 \cdot \mathcal{L}_2(Y_2', Y_2|X;\theta) \\ & + k_3 \cdot \mathcal{L}_3(Y_3', Y_3|X;\theta) \\ & + k_4 \cdot \mathcal{L}_4(Y_4', Y_4|X;\theta) \end{aligned} \quad (1)$$

where θ denotes the parameters of the RU-net, and X denotes the input images. Y' and Y are the predictions and the corresponding annotated ground truth images, with the subscripts

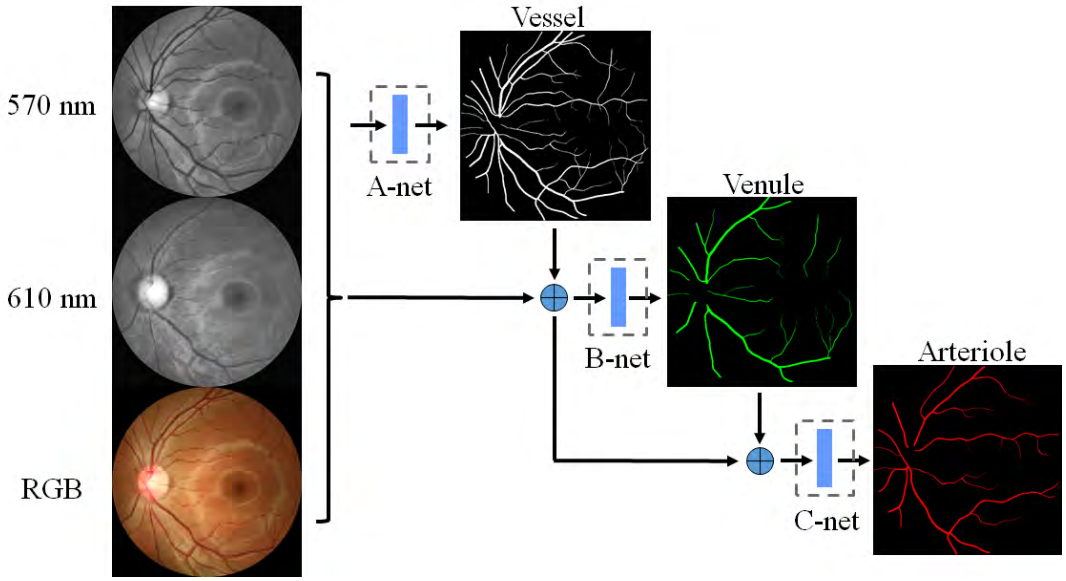

FIGURE 4. The overview structure of the CRU-net.

(1, 2, 3 and 4) to identify different scales (576×576, 288×288, 144×144 and 72×72 pixels). $\mathcal{L}_i$ represents multi-scale losses, and k_i is the weight to balance the losses of different scales. In general, higher values should be assigned to k_is corresponding to the semantic segmentation maps with higher resolution [30]. We experimented different k_i and achieved the best performance with $k1 = 0.3, k2 = 0.25, k3 = 0.2$ and $k4 = 0.15$. For each loss term $\mathcal{L}_i(Y_i', Y_i|X;\theta)$, it is defined as:

$$\begin{aligned}\mathcal{L}_i(Y_i', Y_i|X;\theta) = &-\beta \sum_{j\in Y_+} \log P(y_j = 1|X;\theta) \\ &-(1-\beta)\sum_{j\in Y_-} \log P(y_i = 0|X;\theta), \\ &i \in \{1, 2, 3, 4\} \end{aligned} \tag{2}$$

where Y_+ and Y_- represent the pixel sets that are labeled positive and negative in the annotated ground truth image, respectively. The y_j denotes the label of the pixel j. β is the weight of the loss that is used to balance the losses from the positive and negative samples. We scanned different β values from 0.6 to 0.95 and achieved the best performance with β of 0.9.

C. CASCADE REFINED U-NET (CRU-NET)

The CRU-net consists of three sub-networks (A-, B-, and C-net), each of which is an RU-net (Fig. 4). At the first stage, the A-net focuses on the detection of all the vessels without classifying the vessel types. The A-net takes the RGB image only or together with the 570 nm and 610 nm images as the inputs. The output of the A-net is the prediction of the blood vessels. The loss function of the A-net is defined as:

$$\mathcal{L}_A = \mathcal{L}_{vessel}(Y_{vessel}|X;\theta_A) \tag{3}$$

where θ_A denotes the parameters of the A-net, X denotes the input, and Y_{vessel} represents the ground truth of the vessels.

The objective at the second stage is to segment the venules with reference of all the predicted vessels from the A-net. The input of the B-net is the sum (concatenation) of the input and output of the A-net (Y'_{vessel}). The loss function of B-net is:

$$\mathcal{L}_B = \mathcal{L}_{venule}(Y_{venule}|X, Y'_{vessel};\theta_B) \tag{4}$$

where θ_B represents the parameters of the B-net, Y'_{vessel} is the output of the A-net, and Y_{venule} is the ground truth image of the venule.

At the third stage, the C-net is designed to process the most challenging arteriole segmentation. The input of the C-net is the concatenation of the original input and the outputs from the A-net and the B-net. The output is the segmentation of the arteriole. The loss function of the C-net is:

$$\mathcal{L}_C = \mathcal{L}_{arteriole}(Y_{arteriole}|X, Y'_{vessel}, Y'_{venule};\theta_C) \tag{5}$$

where θ_C denotes the parameters of C-net. $Y_{arteriole}$ is the ground truth image of the arteriole, Y'_{venule} is the prediction of the B-net.

The total loss of the CRU-net is the sum of the three loss terms:

$$\begin{aligned}&\mathcal{L}_{total}(Y_{vessel}, Y_{venule}, Y_{arteriole}|X;\theta) \\ &\quad = w_1 \cdot \mathcal{L}_{vessel}(Y_{vessel}|X;\theta_A) \\ &\qquad + w_2 \cdot \mathcal{L}_{venule}(Y_{venule}|X, Y'_{vessel};\theta_B) \\ &\qquad + w_3 \cdot \mathcal{L}_{arteriole}(Y_{arteriole}|X, Y'_{vessel}, Y'_{venule};\theta_C)\end{aligned} \tag{6}$$

where w_i is to balance the three different loss terms with $\sum_i^3 w_i = 1$. Experimentally, we achieved the best performance with $w_1 = 0.3, w_2 = 0.35$, and $w_3 = 0.35$. Higher weights are assigned to arterioles and venules segmentation tasks as we emphasize the spatial accuracy of the two tasks [30].

TABLE 2. Definitions of the evaluation metrics.

Measure	Mathematical Formula
Accuracy	$(TP+TN)/(TP+TN+FN+FP)$
Sensitivity	$TP/(FN+TP)$
Specificity	$TN/(FP+TN)$
Precision	$TP/(FP+TP)$
F1-Score	$2*TP/(2*TP+FP+FN)$
MCC	$\frac{TP\times TN-FP\times FN}{\sqrt{(FP+TP)(FN+TP)(FP+TN)(FN+TN)}}$

TP stands for true positive; FP: false positve; TN: true negtive; FN: false negative.

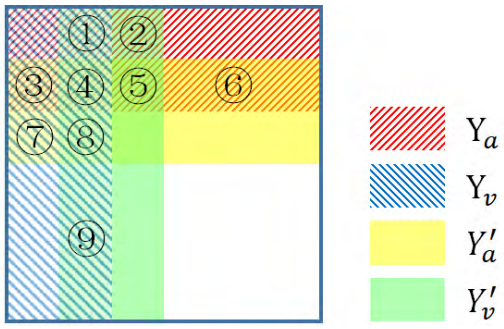

FIGURE 5. The illustration of all the situation of points in the fundus image. Y_v, Y_a denoted the points which were annotated as venule and arteriole, respectively. Y'_v and Y'_a represented the points which were predicted as venule and arteriole, respectively.

D. EVALUATION METRICS

To assess the segmentation performance, we applied the pixel level evaluation on the entire retinal images. We directly counted the number of pixels that were correctly classified or misclassified. We computed the accuracy, sensitivity, specificity, precision, F1-score, and Matthews correlation coefficient (MCC) according to the equations defined in Table 2.

To evaluate the segmentation performance on the venules, TP and TN are the numbers of the pixels which are correctly predicted as venules and background (non-venule), respectively. FP and FN stand for the pixels that are misclassified as the venules and background (non-venule), respectively. A similar interpretation of the symbols applied for the arteriole segmentation.

Differentiating venules and arterioles from the vessels is also a classification problem. Therefore, we quantify the performance of the classifier. Fig. 5 shows all the possible situations of the pixels in the arteriole and venule segmentation experiment. Y_v, Y_a denote the pixels that are annotated as venules and arterioles, respectively. Y'_v and Y'_a represent the pixels that are predicted as venules and arterioles, respectively. Pixels 1, 4, 8 and 9 are venule pixels that are correctly predicted; pixels 3, 4, 5 and 6 are arteriole pixels that are correctly classified as arterioles; pixel 2 is an arteriole pixel that is misclassified as a venule pixel; pixel 7 is a venule pixel that is misclassified as an arteriole.

We define the misclassification rate of arterioles ($MISC_a$) and venules ($MISC_v$). $MISC_a$ is defined as the rate of arteriole that is misclassified as venule. Similarly, $MISC_v$ is defined as the rate of venule that is misclassified as arteriole.

$$MISC_v = \frac{FP_a}{TP_v + FP_a} \tag{7}$$

$$MISC_a = \frac{FP_v}{TP_a + FP_v} \tag{8}$$

We also define the Matthews correlation coefficients for the venule and arteriole as following:

$$\begin{aligned} MCC_v = {} & (TP_v \times TN_v - FP_v \times FN_v)/ \\ & (\sqrt{FP_v + TP_v} \times \sqrt{FN_v + TP_v} \\ & \times \sqrt{FP_v + TN_v} \times \sqrt{FN_v + TN_v}) \end{aligned} \tag{9}$$

$$\begin{aligned} MCC_a = {} & (TP_a \times TN_a - FP_a \times FN_a)/ \\ & (\sqrt{FP_a + TP_a} \times \sqrt{FN_a + TP_a} \\ & \times \sqrt{FP_a + TN_a} \times \sqrt{FN_a + TN_a}) \end{aligned} \tag{10}$$

where TP_v denotes the true positive of venule pixels (pixels 1, 4, 8 and 9 in Fig. 5); FP_v, FN_v and TN_v represent the false positive (pixel 2), false negative (pixel 7) and true negative (pixel 3, 5 and 6) of the venules; TP_a denotes the true positive of arterioles (pixels 3, 4, 5 and 6); FP_a, FN_a and TN_a represent false positive (pixel 7), false negative (pixel 2) and true negative (pixel 1, 8 and 9) of the arteriole. The accuracy of arteriole and venule classification on the correctly detected vessels is defined as:

$$\begin{aligned} Acc &= 1 - \frac{FP_v + FP_a}{TP_v + TP_a + FP_v + FP_a - S_4} \\ &= 1 - \frac{S_2 + S_7}{\sum_{i=1}^{9} S_i} \end{aligned} \tag{11}$$

where S_i denotes pixel i in Fig. 5.

E. NETWORK TRAINING AND TESTING

Image preprocessing was applied before training of the networks. The images were first cropped with a rectangle to remove the black margin and then resized to 576×576 pixels. The same procedures were applied to the ground truth images.

On the DRIVE dataset, to compare the performance of the U-net, RU-net and the CRU-net, we applied the 5-fold cross-validation method. The 40 images were split into 5 subsets with equal size. For each experiment condition, we performed 5 experiments to ensure that each subset was used as a test set and the remains as the training set.

On the DualModal2019 dataset, we performed two different experiments. For the first experiment, we applied only the RGB images from the dataset and compared the performances of the U-net, RU-net, and CRU-net. For the second experiment, we used the dual-modal images (RGB image, 570 nm, and 610 nm images) to compare the performances of the three networks. In addition, we compared the performance of the same network with two different inputs, i.e. RGB images only or dual-modal images to evaluate how the addition of 570 nm and 610 nm monochromic images improve the performance of the networks.

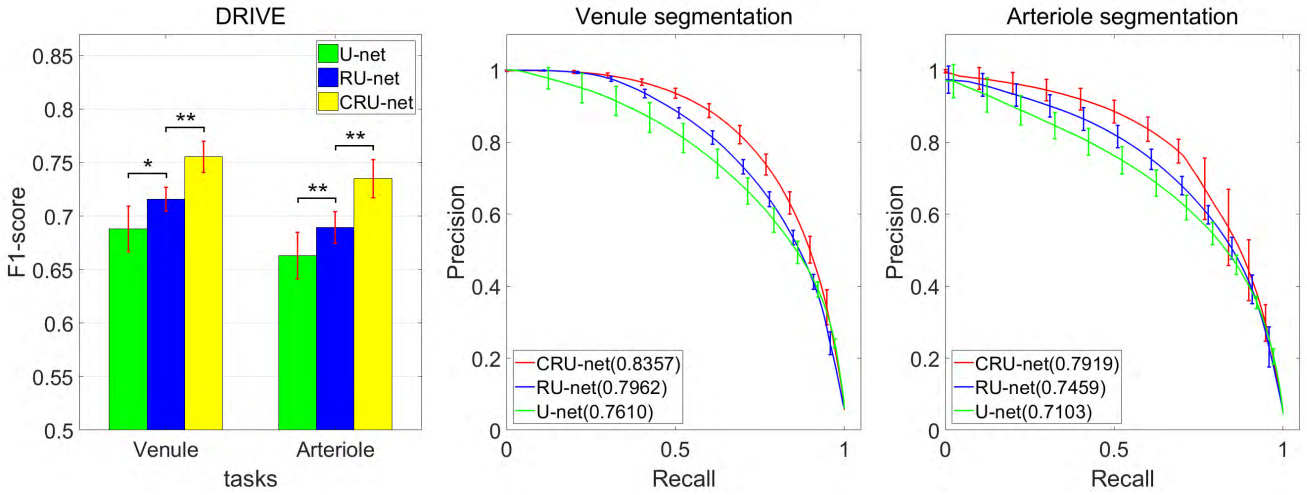

FIGURE 6. The experiment results on the DRIVE dataset. (a)The comparison of F1-score for the venule and arteriole segmentation results of the U-net, RU-net, and CRU-net on the DRIVE dataset. Different colors represented the three different networks. *: p-value < 0.5, and * *: p-value < 0.01. (b) and (c) were the PR-curves of the U-net, RU-net, and CRU-net on the venule and arteriole segmentation tasks trained using the DRIVE dataset with 5-fold cross validation.

TABLE 3. Comparison of the performance of the U-net and RU-net and CRU-net on the DRIVE dataset.

Task	Method	F1-score	MCC	Sensitivity	Precision	Accuracy	Specificity
Venule	U-net	68.81% ±2.14%	67.06% ±2.25%	70.27% ±1.61%	67.44% ±2.95%	96.63% ±0.27%	98.10% ±0.23%
	RU-net	71.57% ±1.11%	70.01% ±1.15%	70.90% ±1.20%	72.28% ±1.68%	97.03% ±0.08%	98.48% ±0.10%
	CRU-net	**75.54% ±1.47%**	**74.25% ±1.52%**	**73.41% ±1.62%**	**77.79% ±1.39%**	**97.49% ±0.13%**	**98.83% ±0.06%**
Arteriole	U-net	66.31% ±2.16%	64.80% ±2.22%	69.74% ±1.82%	63.30% ±3.68%	96.89% ±0.33%	98.13% ±0.32%
	RU-net	68.94% ±1.50%	67.51% ±1.60%	70.59% ±0.59%	67.40% ±2.49%	97.21% ±0.29%	98.43% ±0.24%
	CRU-net	**73.50% ±1.79%**	**72.29% ±1.84%**	**73.64% ±2.09%**	**73.41% ±2.55%**	**97.67% ±0.19%**	**98.77% ±0.19%**

The networks were implemented in Python 3.6 using Keras with TensorFlow as backend. All experiments were performed on a cluster with 10 GeForce GTX 1080Ti GPUs. We initialized all the convolutional layers with the built-in Keras glorot uniform initializer, and the biases were initialized with 0. During training, we applied data augmentation by rotating the image with a random angle between 0° and 360°, flipping left or right randomly and adding random Gaussian noise ($\mathcal{N}(0, 0.2)$) to the images. Besides, all the images were normalized by subtracting the mean pixel value of each channel of the image followed by dividing the corresponding standard deviation. We achieves the networks for 1000 epochs with a batch size of 2, an Adam optimizer with a learning rate of 0.001 and β_1 of 0.5.

IV. EXPERIMENTAL RESULTS

In this section, we first demonstrate that the CRU-net and RU-net outperform U-net on the venule and arteriole segmentations as tested on the DRIVE dataset. The CRU-net achieves the best performance. On the Dualmodal2019 dataset, with only the RGB images as the input, we draw the same conclusion. Then we illustrate that with the additional input of the 570 nm and 610 nm images all the three networks show significant improvement of performance.

A. BOTH CRU-NET AND RU-NET OUTPERFORM THE U-NET ON THE DRIVE DATASET

We conducted the venule and arteriole segmentation experiments on the DRIVE dataset using the U-net, RU-net, and the CRU-net. The results are listed in Table 3.

Since F1-score is a more comprehensive index to evaluate the network performance, we draw the bar graphs using the F1-score in Fig. 6 (a). From both Table 3 and Fig. 6 (a), it is clear that both the RU-net and CRU-net significantly outperform the U-net. The F1-scores of the RU-net are 2.76% and 2.63% higher than those of the U-net on the venule and arteriole segmentations, respectively. The F1-scores of the CRU-net are more than 6.73% and 7.19% higher than

TABLE 4. The 5-fold cross validation experiment results of U-net, RU-net, and CRU-net on DualModal2019 dataset with only RGB inputs.

Task	Method	F1-score	MCC	Sensitivity	Precision	Accuracy	Specificity
Venule	U-net	74.37% ±3.58%	73.52% ±3.63%	74.64% ±2.38%	74.30% ±5.93%	98.26% ±0.30%	99.08% ±0.30%
	RU-net	76.09% ±3.33%	75.29% ±3.40%	76.20% ±3.19%	76.13% ±4.96%	98.38% ±0.26%	99.15% ±0.25%
	CRU-net	**77.64% ±3.56%**	**76.88% ±3.63%**	**78.50% ±1.87%**	**76.88% ±5.32%**	**98.47% ±0.29%**	**99.17% ±0.25%**
Arteriole	U-net	72.43% ±1.95%	71.58% ±1.92%	71.86% ±2.19%	73.04% ±2.42%	98.33% ±0.16%	99.17% ±0.08%
	RU-net	74.24% ±1.76%	73.47% ±1.73%	72.81% ±1.88%	75.75% ±2.01%	98.46% ±0.16%	99.27% ±0.07%
	CRU-net	**76.55% ±2.81%**	**75.82% ±2.83%**	**76.23% ±3.23%**	**76.89% ±2.69%**	**98.58% ±0.17%**	**99.28% ±0.07%**

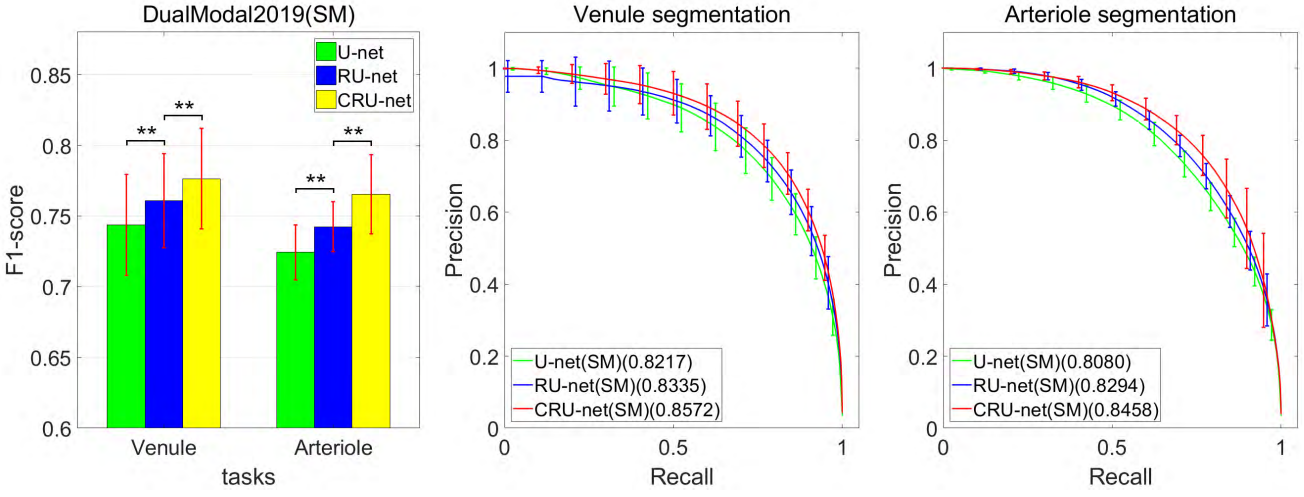

FIGURE 7. The 5-fold cross validation experiment results of U-net, RU-net, and CRU-net trained on DualModal2019 dataset with only inputting fundus RGB images. (a)The comparison of the F1-score of U-net, RU-net, and CRU-net on the venule and arteriole segmentation. (b) and (c) shown the PR-curves of the venule and arteriole segmentation for U-net, RU-net, and CRU-net. 'SM': Networks were trained with only RGB images.

those achieved by the U-net. MCCs have the same trend as F1-scores as shown in Table 3.

Fig. 6 (b, c) show the precision-recall (PR) curves of the 5-fold cross validation experiments for the venule and arteriole segmentations, respectively. The PR-curve of the CRU-net and RU-net enclose the curve of the U-net, suggesting the better performance of the CRU-net and RU-net. The AUC of the RU-net on venule and arteriole segmentation are 0.7962 and 0.7459, respectively. The CRU-net has the largest AUCs of 0.8357 and 0.7919.

B. THE CRU-NET AND RU-NET OUTPERFORM THE U-NET ON THE DUALMODAL2019 DATASET

We conducted 5-fold cross-validation experiments on the DualModal2019 dataset with two different experimental conditions.

In the first experiment, the networks were trained only with the RGB images as the input, without using the 570 nm and 610 nm monochromic images. We wanted to further test the performance of the networks. The results are shown in Table 4 and Figure 7. The F1-scores of the RU-net are 1.72% and 1.81% higher than U-net on the venule and arteriole segmentation; the F1-scores of the CRU-net were 3.27% and 4.12% higher than those of the U-net. A similar trend is found for the MCCs. Fig. 7(a) show that both the RU-net and CRU-net outperform the U-net, and the CRU-net achieved the best performance. Fig. 7(b) and Fig. 7(c) are the PR-curves of the three networks. In both cases, the PR-curves of the CRU-net completely encloses those of the other two networks, suggesting the best performance. The RU-net achieves better performance than the U-net as

TABLE 5. The 5-fold cross validation experiment results of U-net, RU-net, and CRU-net on the DualModal2019 dataset with dual-modal inputs.

Method	Task	F1-Score	MCC	Sensitivity	Precision	Accuracy	Specificity
Venule	U-net	77.41% ±2.15%	76.64% ±2.16%	76.69% ±2.46%	78.15% ±2.12%	98.50% ±0.10%	99.25% ±0.06%
	RU-net	78.54% ±1.69%	77.79% ±1.71%	78.86% ±2.27%	78.24% ±1.54%	98.55% ±0.13%	99.23% ±0.09%
	CRU-net	**79.53% ±1.98%**	**78.81% ±2.03%**	**80.07% ±2.14%**	**79.00% ±1.91%**	**98.61% ±0.15%**	**99.26% ±0.07%**
Arteriole	U-net	73.53% ±2.45%	72.71% ±2.43%	73.14% ±2.33%	73.96% ±3.04%	98.39% ±0.16%	99.19% ±0.12%
	RU-net	75.93% ±2.71%	75.18% ±2.74%	75.48% ±2.64%	76.39% ±2.91%	98.54% ±0.18%	99.27% ±0.10%
	CRU-net	**77.69% ±2.68%**	**77.00% ±2.69%**	**76.84% ±3.10%**	**78.56% ±2.37%**	**98.66% ±0.15%**	**99.34% ±0.09%**

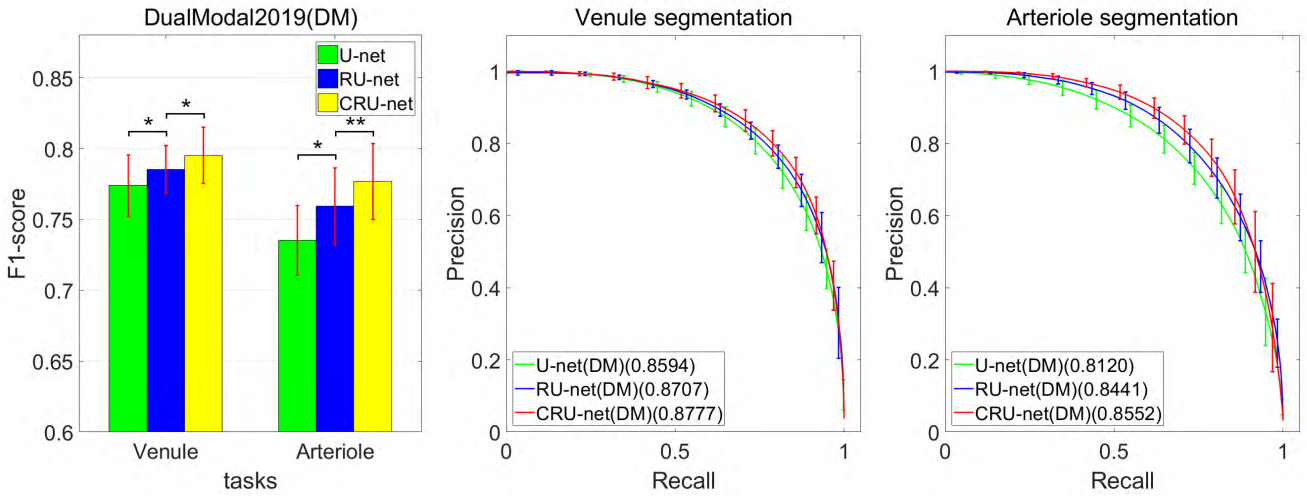

FIGURE 8. The 5-fold cross validation experiment results of U-net, RU-net, and CRU-net trained on DualModal2019 dataset with dual-modal images. (a)The comparison of the F1-score for the venule and arteriole segmentation results of the U-net, RU-net, and CRU-net. (b) and (c) shown the PR-curves of U-net, RU-net, and CRU-net on venule and arteriole segmentation task. 'DM': Networks trained with dual-modal images.

suggested by the PR-curves and the AUC. The conclusion of this experiment is consistent with the test on the DRIVE dataset.

In the second experiment, all the networks were trained on the DualModal2019 dataset with the addition of 570 nm and 610 nm monochromic images. As shown in Table 5, the F1-scores of the RU-net are 1.13% and 2.4% higher than U-net on the venule and arteriole segmentation, and the F1-scores of the CRU-net are 2.12% and 4.16% higher than U-net. As shown in Fig. 8(a), the CRU-net achieves the best performance and the RU-net shows better performance than the U-net. The PR-curves of the CRU-net completely enclose those of the RU-net and the U-net (Fig. 8(b, c)), and the AUCs of the CRU-net and RU-net are larger than those of the U-net.

C. ADDITION OF 570 NM AND 610 NM IMAGES IMPROVES THE SEGMENTATION PERFORMANCE

To verify whether the addition of dual-modal images improves the performance of the networks, we compare the results of the two experimental conditions on the three networks. As shown in Fig. 9, for both the venule and arteriole segmentations, all the three networks achieve higher F1-scores when trained with dual-modal images than trained only with RGB images.

D. DUAL-MODAL IMAGES SIGNIFICANTLY IMPROVE THE CLASSIFICATION ACCURACY

We evaluated the misclassification rates, Matthews correlation coefficient, and classification accuracy as defined by

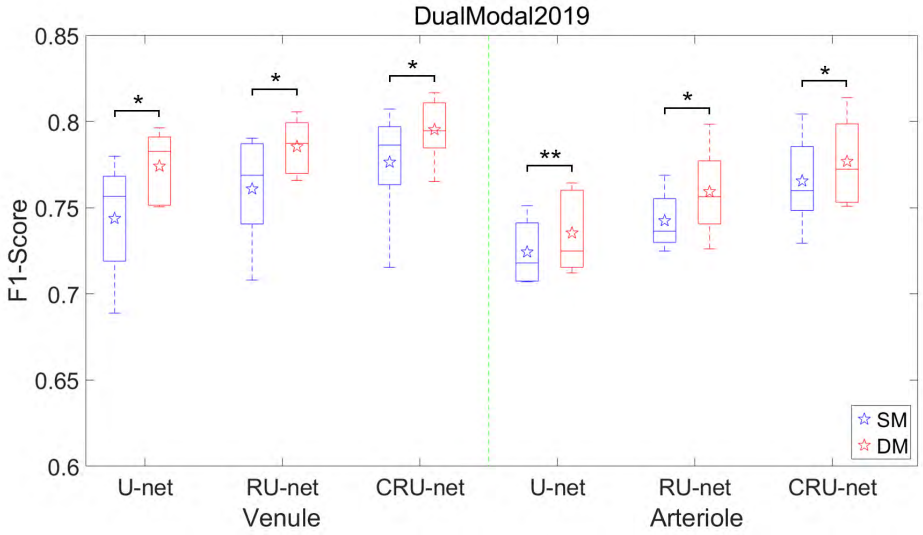

FIGURE 9. Comparisons of the network performance trained using the RGB only versus trained with dual-modal images (RGB, 570 nm, and 610 nm images) on the DualModal2019 dataset.

TABLE 6. The misclassification rates and accuracy on the DRIVE and DualModal2019 datasets.

method	$MISC_v$	$MISC_a$	Acc	MCC_v	MCC_a
U-net(DRIVE)	9.48%	5.73%	91.99%	83.92%	84.06%
RU-net(DRIVE)	7.57%	5.12%	93.37%	86.63%	86.75%
CRU-net(DRIVE)	7.09%	4.41%	93.97%	87.87%	87.97%
CRU-net_SM(DualModal2019)	3.64%	3.94%	96.20%	92.37%	92.38%
CRU-net_DM(DualModal2019)	**1.93%**	**3.59%**	**97.27%**	**94.53%**	**94.53%**

Eq. (7), Eq. (8) Eq. (9), Eq. (10), and Eq. (11). As shown in Table 6, on the DRIVE dataset, both RU-net and CRU-net achieve much lower $MISC_v$ and $MISC_a$, higher MCC_v and MCC_a, and higher Acc than the U-net. The misclassification rate of the venules achieved by the CRU-net is more than 2% lower than the U-net, and the Acc is 1.98% higher. Similarly, MCC_v and MCC_a are 3.95% and 3.91% higher, respectively.

On the DualModal2019 dataset, we compared the performance of the CRU-net trained only with RGB images (labeled as CRU-net_SM in the table) with the CRU-net trained with dual-modal images (labeled as CRU-net_DM). With the dual-modal images, the misclassification rate of the venules decreases from 3.64% to 1.93%, and the Acc increases more than 1%. Both MCC_v and MCC_a increase more than 2%.

V. DISCUSSION

Accurate segmentation of the arteriole and venule is important in the diagnosis of many diseases. In this study, we sought to develop a deep convolutional neural network (DCNN) based method for automatic arteriovenous detection and segmentation. To alleviate the difficulties of previous studies, we 1) applied dual-modal images, which acquired much more information on the venule and arteriole than conventional color fundus images; 2) constructed a refined U-net (RU-net) and a cascade RU-net (CRU-net), both of which showed superior performance on the arteriovenous segmentation.

The proposed RU-net significantly improves arteriovenous segmentation as shown in Table 3 and 4. The RU-net (Fig 3) is based on the conventional U-net [23] but with significant modifications. First, we applied a multi-scale loss structure. In the decoder path, a scale loss was evaluated for each upsampling step. Multi-scale losses alleviate vanishing gradient problem to facilitate the learning process of the network [35]. Also, applying multi-scale losses is equivalent to applying multiple supervisors. Second, as marked with the blue dotted box shown in Fig. 3, the upsampling feature maps are the outputs of convolution operations instead of the segmentation map. The feature maps from the convolution operations can retain more features to prevent feature loss in the decoder path. Third, we applied a convolution operation (marked with a red dotted box in Fig. 3) before the feature maps from the encoding path were concatenated into the decoding path. This configuration helps to transfer low dimensional features to the higher dimensional space.

The CRU-net further improves the arteriovenous segmentation. It comprises three sub-networks (Fig 4), each of which is an RU-net. The first subnetwork (A-net) gets the overall vessel segmentation, which is part of the input of the following B-net and C-net, providing prior vessel information. The B-net focuses on the venule segmentation, which is easier

TABLE 7. Comparison of the classification accuracy with previous methods on the DRIVE dataset.

Methods	Year	Acc	Description
Niemeijer *et al.* [31]	2009	88%(AUC)	Method evaluated on known vessel centerlines
Mirsharif *et al.* [32]	2011	86%	Method evaluated on selected major vessels and main branches
Estrada *et al.* [16]	2014	87.4%	Method developed and evaluated on known vessel centerline locations
Xu *et al.* [33]	2017	83.2%	Method evaluated on all correctly detected vessels
Xu *et al.* [34]	2018	90.0%	Method evaluated on automatically detected vessels
Proposed method	**2019**	**93.97%**	**Method evaluated on automatically detected vessels**

than the arteriole segmentation. The C-net targets on the most difficult task of arteriole segmentation. The three tasks are nested and mutually reinforcing. Compared with the U-net and RU-net, the CRU-net is an integrated architecture that combines the vessel and arteriovenous segmentation. It maximizes the utilization of the correlation information among the three tasks and significantly improves the performance of the network. This differs from most of the published work, where vessel segmentation and arteriovenous classification are two-step process [13], [21], [22], ignoring the correlations among the tasks.

We listed our results with published studies on the arteriole and venule detection and segmentation in Table. 7. However, one should note that a direct comparison of the methods is not possible because the evaluation indices used in different studies are different. For example, in reference [16], [31], the accuracy was defined on the known vessel centerlines, while in reference [34] it was defined on the known vessels. Therefore, we listed the studies and provided a brief description of the methods applied in the studies.

Dual-modal images improve the CRU-net network performance, particularly on the segmentation of the arterioles. Dual-modal images contain much more information than conventional RGB fundus images. The contrast of the venules in the 610 nm wavelength images is much higher than the arterioles, helpful for differentiating arterioles and venules. In this paper, we applied the RGB, 610 nm and 570 nm wavelength images as input to train CRU-net. Compared with the network trained with only RGB images, the features extracted from RGB, 570 nm and 610 nm images are much more distinguishable, significantly reducing the misclassification rate of the arterioles and venules.

On average, it took two hundred and twenty, two hundred and four, and three hundred and forty-three minutes to train the U-net, RU-net, and CRU-net on the DRIVE dataset on a GeForce GTX 1080Ti GPU, respectively. However, to segment both the arterioles and the venules, we need to train the U-net and RU-net twice, one time on the arteriole and another time on the venule segmentations. Therefore, the total training time for CRU-net is much less than RU-net and U-net. To process an image, the U-net, RU-net, and CRU-net all took about 350 milliseconds. In total, the CRU-net has about 5.57M parameters to train, while the U-net and RU-net have 1.95M and 1.86M parameters, respectively.

As demonstrated in the study, the dual-modal fundus images provide much more information about the venules and arterioles. In combination with a properly designed network, we can fully utilize the information to improve arteriovenous analysis. However, the current limitation is that dual-modal fundus cameras are not as widely used as conventional fundus cameras. Therefore, the data is limited. Considering the advantages of the dual-modal fundus cameras, we expect it to be more widely adopted in the future.

VI. CONCLUSION

In the study, we constructed a CRU-net, which fully took advantages of the dual-modal fundus images to detect and segment the arterioles and venules simultaneously. Dual-modal fundus images provide much richer information about the retina. For example, retinal oxygen saturation level can be evaluated by using the 570 nm and 610 nm monochromic images. In combination with the developed CRU-net, we will be able to quantitatively analyze the oxygen saturation level in arterioles and venules, which is related to many diseases. For example, recent studies [36], [37] show a significant difference in the oxygen saturation level of Alzheimer's patients and healthy populations. In addition, we expect that ophthalmic diseases, such as diabetic retinopathy, retinal vein occlusion (RVO) and ischemic optic neuropathy (ION), which have different effects on arterioles and venules to take advantages of the dual-modal fundus imaging technique and our accurate arteriovenous analysis.

Besides, one of the common difficulties in deep learning study is the lack of high-quality data, especially expert labeled data. We make our DualModal2019 dataset, together with the manually annotated ground truth images, publicly available upon publication of the study so that more researchers can explore it. We expect more studies and better algorithms to come.

REFERENCES

[1] T. Y. Wong *et al.*, "Retinal arteriolar narrowing and risk of coronary heart disease in men and women the atherosclerosis risk in communities study," *Jama*, vol. 287, no. 9, pp. 1153–1159, Mar. 2002.

[2] T. Y. Wong *et al.*, "Retinal vascular caliber, cardiovascular risk factors, and inflammation: The multi-ethnic study of atherosclerosis (MESA)," *Investigative Ophthalmology Vis. Sci.*, vol. 47, no. 6, pp. 2341–2350, Jun. 2006.

[3] T. T. Nguyen and T. Y. Wong, "Retinal vascular changes and diabetic retinopathy," *Current Diabetes Rep.*, vol. 9, no. 4, pp. 277–283, Aug. 2009.

[4] G. D. Joshi, J. Sivaswamy, and S. Krishnadas, "Optic disk and cup segmentation from monocular color retinal images for glaucoma assessment," *IEEE Trans. Med. Imag.*, vol. 30, no. 6, pp. 1192–1205, Jun. 2011.
[5] L. S. Lim, P. Mitchell, J. M. Seddon, F. G. Holz, and T. Y. Wong, "Age-related macular degeneration," *Lancet*, vol. 379, no. 9827, pp. 1728–1738, 2012.
[6] J. Flamme, K. Konieczka, R. M. Bruno, A. Virdis, A. J. Flammer, and S. Taddei, "The eye and the heart," *Eur. Heart J.*, vol. 34, no. 17, pp. 1270–1278, May 2013.
[7] K. McGeechan *et al.*, "Meta-analysis: Retinal vessel caliber and risk for coronary heart disease," *Ann. Internal Med.*, vol. 151, no. 6, pp. 404–413, Sep. 2009.
[8] A. Grosso, F. Veglio, M. Porta, F. Grignolo, and T. Wong, "Hypertensive retinopathy revisited: Some answers, more questions," *Brit. J. Ophthalmology*, vol. 89, no. 12, pp. 1646–1654, Dec. 2005.
[9] T. Kamisawa, N. Egawa, H. Nakajima, K. Tsuruta, A. Okamoto, and N. Kamata, "Clinical difficulties in the differentiation of autoimmune pancreatitis and pancreatic carcinoma," *Amer. J. Gastroenterology*, vol. 98, no. 12, pp. 2694–2699, Dec. 2003.
[10] B. Dashtbozorg, A. M. Mendonça, and A. Campilho, "An automatic method for the estimation of arteriolar-to-venular ratio in retinal images," in *Proc. 26th IEEE Int. Symp. Comput.-Based Med. Syst.*, Jun. 2013, pp. 512–513.
[11] M. K. Ikram *et al.*, "Are retinal arteriolar or venular diameters associated with markers for cardiovascular disorders? the rotterdam study," *Investigative Ophthalmology Vis. Sci.*, vol. 45, no. 7, pp. 2129–2134, Jul. 2004.
[12] E. Van Kampen and W. Zijlstra, "Spectrophotometry of hemoglobin and hemoglobin derivatives," *Adv. Clin. Chem.*, vol. 23, pp. 199–257, Apr. 1983.
[13] R. Welikala *et al.*, "Automated arteriole and venule classification using deep learning for retinal images from the UK Biobank cohort," *Comput. Biol. Med.*, vol. 90, pp. 23–32, Nov. 2017.
[14] E. Grisan and A. Ruggeri, "A divide et impera strategy for automatic classification of retinal vessels into arteries and veins," in *Proc. 25th Annu. Int. Conf. IEEE Eng. Med. Biol. Soc.*, vol. 1, Sep. 2003, pp. 890–893.
[15] K. Rothaus, X. Jiang, and P. Rhiem, "Separation of the retinal vascular graph in arteries and veins based upon structural knowledge," *Image Vis. Comput.*, vol. 27, no. 7, pp. 864–875, Jun. 2009.
[16] B. Dashtbozorg, A. M. Mendonça, and A. J. Campilho, "An automatic graph-based approach for artery/vein classification in retinal images," *IEEE Trans. Image Process.*, vol. 23, no. 3, pp. 1073–1083, Mar. 2014.
[17] M. Havaei *et al.*, "Brain tumor segmentation with deep neural networks," *Med. Image Anal.*, vol. 35, pp. 18–31, Jan. 2017.
[18] J.-Z. Cheng *et al.*, "Computer-aided diagnosis with deep learning architecture: Applications to breast lesions in US images and pulmonary nodules in CT scans," *Sci. Rep.*, vol. 6, Apr. 2016, Art. no. 24454.
[19] S. Liu, S. Liu, W. Cai, S. Pujol, R. Kikinis, and D. Feng, "Early diagnosis of alzheimer's disease with deep learning," in *Proc. 11th Int. Symp. Biomed. Imag. (ISBI)*, Apr./May 2014, pp. 1015–1018.
[20] R. Zheng *et al.*, "Detection of exudates in fundus photographs with imbalanced learning using conditional generative adversarial network," *Biomed. Opt. Express*, vol. 9, no. 10, pp. 4863–4878, Oct. 2018.
[21] R. Hemelings, B. Elen, I. Stalmans, K. Van Keer, P. De Boever, and M. B. Blaschko, "Artery-vein segmentation in fundus images using a fully convolutional network," in *Proc. 1st Conf. Med. Imag. Deep Learn. (MIDL)*, Apr. 2018.
[22] X. Xu, T. Tan, and F. Xu, "An improved U-net architecture for simultaneous arteriole and venule segmentation in fundus image," in *Proc. Annu. Conf. Med. Image Understand. Anal.* Southampton, U.K.: Springer, Aug. 2018, pp. 333–340.
[23] O. Ronneberger, P. Fischer, and T. Brox, "U-net: Convolutional networks for biomedical image segmentation," in *Proc. Int. Conf. Med. Image Comput. Comput.-Assist. Intervent*. Munich, Germany: Springer, Nov. 2015, pp. 234–241.
[24] M. I. Meyer, A. Galdran, P. Costa, A. M. Mendonça, and A. Campilho, "Deep convolutional artery/vein classification of retinal vessels," in *Proc. Int. Conf. Image Anal. Recognit.* Povoa de Varzim, Portugal: Springer, Jun. 2018, pp. 622–630.
[25] S. AlBadawi and M. Fraz, "Arterioles and venules classification in retinal images using fully convolutional deep neural network," in *Proc. Int. Conf. Image Anal. Recognit.* Povoa de Varzim, Portugal: Springer, Jun. 2018, pp. 659–668.
[26] V. Badrinarayanan, A. Kendall, and R. Cipolla. (2015). "Segnet: A deep convolutional encoder-decoder architecture for image segmentation." [Online]. Available: https://arxiv.org/abs/1511.00561
[27] J. Staal, M. D. Abràmoff, M. Niemeijer, M. A. Viergever, and B. Van Ginneken, "Ridge-based vessel segmentation in color images of the retina," *IEEE Trans. Med. Imag.*, vol. 23, no. 4, pp. 501–509, Apr. 2004.
[28] T. A. Qureshi, M. Habib, A. Hunter, and B. Al-Diri, "A manually-labeled, artery/vein classified benchmark for the drive dataset," in *Proc. 26th IEEE Int. Symp. Comput.-Based Med. Syst.*, Jun. 2013, pp. 485–488.
[29] M. A. Islam, S. Naha, M. Rochan, N. Bruce, and Y. Wang. (2017). "Label refinement network for coarse-to-fine semantic segmentation." [Online]. Available: https://arxiv.org/abs/1703.00551
[30] R. Ranjan, V. M. Patel, and R. Chellappa, "Hyperface: A deep multi-task learning framework for face detection, landmark localization, pose estimation, and gender recognition," *IEEE Trans. Pattern Anal. Mach. Intell.*, vol. 41, no. 1, pp. 121–135, Jan. 2019.
[31] M. Niemeijer, B. van Ginneken, and M. D. Abràmoff, "Automatic classification of retinal vessels into arteries and veins," Proc. SPIE, vol. 7260, Feb. 2009, Art. no. 72601F.
[32] G. Mirsharif, F. Tajeripour, F. Sobhanmanesh, H. Pourreza, and T. Banaee, "Developing an automatic method for separation of arteries from veins in retinal images," in *Proc. 1st Int. Conf. Comput. Knowl. Eng. (ICCKE)*, Oct. 2011, pp. 202–207.
[33] X. Xu, W. Ding, M. D. Abràmoff, and R. Cao, "An improved arteriovenous classification method for the early diagnostics of various diseases in retinal image," *Comput. Methods Programs Biomed.*, vol. 141, pp. 3–9, Apr. 2017.
[34] X. Xu *et al.*, "Simultaneous arteriole and venule segmentation with domain-specific loss function on a new public database," *Biomed. Opt. Express*, vol. 9, no. 7, pp. 3153–3166, Jul. 2018.
[35] C. Szegedy *et al.*, "Going deeper with convolutions," in *Proc. IEEE Conf. Comput. Vis. Pattern Recognit.*, Jun. 2015, pp. 1–9.
[36] A. B. Einarsdottir, S. H. Hardarson, J. V. Kristjansdottir, D. T. Bragason, J. Snaedal, and E. Stefánsson, "Retinal oximetry imaging in alzheimer's disease," *J. Alzheimer's Disease*, vol. 49, no. 1, pp. 79–83, Jan. 2016.
[37] O. B. Olafsdottir *et al.*, "Retinal oxygen metabolism in patients with mild cognitive impairment," *Alzheimer's Dementia, Diagnosis, Assessment Disease Monit.*, vol. 10, pp. 340–345, Mar. 2018.

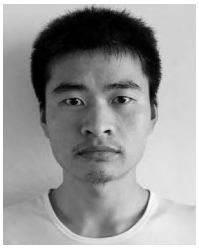

SHULIN ZHANG is currently pursuing the Ph.D. degree with the Department of Precision Machinery and Precision Instrumentation, University of Science and Technology of China (USTC), Hefei, China. His major research interests include machine learning, deep learning neural networks, and medical image processing and their applications in assisted medical diagnosis.

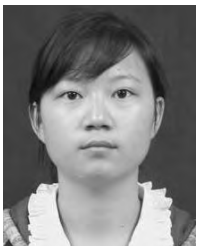

RUI ZHENG is currently pursuing the Ph.D. degree with the Department of Precision Machinery and Precision Instrumentation, University of Science and Technology of China (USTC), Hefei, China. Her major research interests include deep learning, intelligent information processing, computer vision, and medical image processing and their applications in industry.

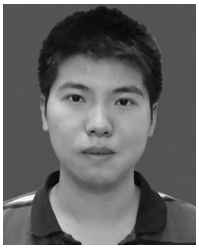

YUHAO LUO is currently pursuing the Ph.D. degree with the Department of Precision Machinery and Precision Instrumentation, University of Science and Technology of China (USTC), Hefei, China. His main research interests include deep learning, intelligent information processing, computer vision, and medical image processing and their applications in industry.

XUEWEI WANG received the M.S. degree from the University of Science and Technology of China, Hefei, China, in 2015, where she is currently pursuing the Ph.D. degree with the Department of Precision Machinery and Precision Instrumentation. Her research interests include image processing, computer vision, and artificial intelligence.

JIANBO MAO is currently a Physician of the Department of Ophthalmology, Eyesight Hospital of Wenzhou Medical University. His research interests include retinopathy of prematurity, macular degeneration, diabetic retinopathy, fundus laser, and angiography.

CYNTHIA J. ROBERTS is currently a Professor with the Department of Ophthalmology and Visual Science, The Havener Eye Institute. She is also a Professor of biomedical engineering, The Ohio State University. She has given over 200 national and international invited lectures. She has published over 120 papers in peer-reviewed journals. She has contributed over 20 book chapters. Her research interests include corneal and ocular biomechanics in cornea, refractive surgery and glaucoma, the *in vivo* measurement of corneal biomechanics, IOP measurement errors, and ophthalmic imaging applications including corneal topography and OCT. She has co-edited two books on corneal topography and corneal biomechanics.

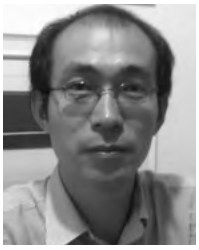

MINGZHAI SUN received the Ph.D. degree in physics from the University of Missouri, Columbia, MO, USA, in 2008. He is currently a Professor with the Department of Precision Machinery and Precision Instrumentation, University of Science and Technology of China (USTC), Hefei, China. His research interests include optical super-resolution microscopy, biomedical device development, and bioimage informatics, particularly in medical image analysis and deep learning-based algorithms.